

Superfluidity in the one-dimensional Bose-Hubbard modelThomas G. Kiely^{✉*} and Erich J. Mueller^{✉†}*Laboratory of Atomic and Solid State Physics, Cornell University, Ithaca, New York 14853, USA*

(Received 1 February 2022; accepted 24 March 2022; published 4 April 2022)

We study superfluidity in the one-dimensional Bose-Hubbard model using a variational matrix product state technique. We determine the superfluid density as a function of the Hubbard parameters by calculating the energy cost of phase twists in the thermodynamic limit. As the system is critical, correlation functions decay as power laws and the entanglement entropy grows with the bond dimension of our variational state. We relate the resulting scaling laws to the superfluid density. We compare two different algorithms for optimizing the infinite matrix product state and develop a physical explanation why one of them (VUMPS) is more efficient than the other (iDMRG). Finally, we comment on finite-temperature superfluidity in one dimension and how our results can be realized in cold-atom experiments.

DOI: [10.1103/PhysRevB.105.134502](https://doi.org/10.1103/PhysRevB.105.134502)**I. INTRODUCTION**

Superfluidity is one of the most spectacular examples of macroscopic quantum coherence. It is a collective effect where some fraction of the fluid flows without dissipation. In a Galilean-invariant system at zero temperature, this superfluid fraction is either 0 or 1 [1]. In a lattice system, however, the superfluid fraction can take on intermediate values. Here we use matrix product state techniques [2] to compute the zero-temperature superfluid fraction of the one-dimensional (1D) Bose-Hubbard model as a function of its parameters: the chemical potential μ , which controls the number of particles; the on-site interaction strength U ; and the tunneling matrix element t . We reproduce the iconic Mott lobes in the $(\mu/t, U/t)$ plane, showing insulating regions where the superfluid fraction vanishes and superfluid regions where it is finite. We connect the superfluid fraction to a number of other properties of the 1D lattice Bose gas.

Superfluidity in one dimension is special. In dimensions $d \geq 3$, superfluidity is usually accompanied by Bose-Einstein condensation, where the off-diagonal elements of the single particle density matrix $\langle \psi^\dagger(r)\psi(r') \rangle$ approach a constant for large spatial separations $|r - r'| \rightarrow \infty$. This is a form of long-range order, corresponding to the spontaneous breaking of a continuous $U(1)$ symmetry. Long-range order of this form is not permitted in one dimension [3,4], so there is no condensation; rather, the density matrix falls off as a power law $\langle \psi^\dagger(r)\psi(r') \rangle \sim (r - r')^{-K/2}$. We implement two variational matrix product state algorithms, which allows us to explicitly calculate these correlation functions in the thermodynamic limit [5–10]. A remarkable feature of one-dimensional superfluidity is that the exponent K can be related to the superfluid density [11,12]. We numerically show this correspondence.

Our technique gives us access to the entanglement spectrum, which characterizes the quantum correlations between different parts of the system. The effective low-energy theory describing the 1D Bose-Hubbard model has a conformal invariance which leads to a scaling behavior of this spectrum [13]. We demonstrate this scaling in our data.

The 1D Bose-Hubbard model is iconic and has been very widely studied. It is described by a Hamiltonian

$$\mathcal{H}_{\text{BH}} = \sum_j \left(-t(a_j^\dagger a_{j+1} + \text{H.c.}) - \mu n_j + \frac{U}{2} n_j(n_j - 1) \right), \quad (1)$$

where a_j are annihilation operators for particles on site j and $n_j = a_j^\dagger a_j$. Unlike its fermionic cousin, the Bose-Hubbard model is not integrable due to the infinitely large local Hilbert space. This has made it a popular target for strong-coupling expansions [14,15] and numerical techniques, such as quantum Monte Carlo (QMC) algorithms [16–18], density matrix renormalization-group methods [19–27], the variational cluster approximation [28,29], exact diagonalization [30], and even machine learning methods [31–33]. These prior works have largely focused on mapping out the phase diagram and in particular identifying the Berezinskii-Kosterlitz-Thouless (BKT) transition point at the Mott lobe tip [34–36]. Calculating the superfluid fraction in this model has traditionally been challenging. A popular approach in the QMC community is to exploit an identity between the superfluid density and the imaginary-time winding number [37]. Density matrix renormalization-group techniques have been used to calculate the superfluid density in finite-length systems by imposing a phase twist to systems with open boundary conditions [19,38] or periodic boundary conditions [27,39]. Our numerical method has some advantages over these prior approaches: We minimize the energy within the space of translationally invariant matrix product states, directly giving us results in the zero-temperature and thermodynamic limit.

*tgk37@cornell.edu

†em256@cornell.edu

In Sec. II we give some required background about Luttinger-liquid theory, which describes the low-energy physics of our system. In Sec. III we more precisely define the superfluid density ρ_s in a 1D system. We note that this definition is itself the subject of some debate and we explain the relevant issues, the consensus, and the operational definition which will be used in this paper. Section IV describes our numerical approach. We introduce two algorithms, iDMRG [6,7], and VUMPS [8]. We describe how to use these techniques to calculate ρ_s and the relevant correlation functions. Section V gives the results of our calculations, including a comparison of the convergence properties of iDMRG and VUMPS. Section VI discusses techniques for measuring superfluid density in 1D systems. We summarize in Sec. VII.

II. LUTTINGER-LIQUID THEORY

Here we review the most pertinent results from Luttinger-liquid theory, as these are essential for our analysis and discussion. Luttinger-liquid theory encompasses the low-energy descriptions of a large variety of interacting 1D systems [40]. For a bosonic system, the low-energy Hamiltonian can be derived [13] by expanding the boson field operators as

$$\psi(x) = \sqrt{\rho_0 - \frac{1}{\pi} \nabla \theta(x)} e^{i\phi(x)}, \quad (2)$$

where ρ_0 is the average number density and $\nabla \theta(x)$ and $\phi(x)$ are canonically conjugate fields corresponding to long-wavelength density and phase fluctuations, respectively. In terms of these fields, the Luttinger-liquid Hamiltonian is of the form

$$\mathcal{H}_{\text{LL}} = \frac{\hbar}{2\pi} \int dx [v_j (\nabla \phi)^2 + v_n (\nabla \theta - \pi \rho_0)^2]. \quad (3)$$

This Hamiltonian describes gapless, long-wavelength fluctuations in the density and phase fields with respective sound velocities v_n and v_j . The velocity of phase fluctuations is $v_j = \frac{\hbar \pi \rho_s}{m}$, where ρ_s is the zero-temperature superfluid density or equivalently the Drude weight (see Sec. III). In a Galilean-invariant system, $\rho_s = \rho_0$ so that v_j is not renormalized by interactions, which is consistent with the aforementioned theorem that the superfluid fraction of a translationally invariant systems is either zero or unity [1]. The velocity of density fluctuations is $v_n = 1/\hbar \pi \kappa$, where $\kappa = \partial \rho_0 / \partial \mu$ is the charge compressibility. It is common practice to reparametrize Eq. (3) in terms of a single sound velocity $u = \sqrt{v_j v_n}$ and the dimensionless Luttinger parameter $K = \sqrt{v_n / v_j}$. Diagonalizing the Hamiltonian with a Bogoliubov transformation yields [13]

$$\mathcal{H}_{\text{LL}} = \hbar \left[\sum_{q \neq 0} \omega_q b_q^\dagger b_q + \left(\frac{\pi}{2L} \right) [v_j J^2 + v_n (N - N_0)^2] \right], \quad (4)$$

where $\omega_q = u|q|$ for small q and b_q (b_q^\dagger) are the Bogoliubov annihilation (creation) operators. We can therefore see that excitations of the Luttinger liquid are sound modes that are a linear combination of density and phase fluctuations. The parameters J and N correspond to the total number of π -phase twists and the total number of particles, respectively, over

the length L of the system. Periodic boundary conditions on the bosonic many-body wave function imply $J \in 2\mathbb{Z}$. The average number of particles is given by N_0 .

The Luttinger liquid has a host of interesting properties. Despite being a bosonic theory, the lack of long-range order in one dimension prevents Bose-Einstein condensation. The propensity to order nonetheless leads to a power-law decay of the single-particle equal-time Green's function $\langle a_i^\dagger a_{i+j} \rangle$ [13,40]:

$$\langle a_i^\dagger a_{i+j} \rangle \approx n_0 (n_0 j)^{-K/2}. \quad (5)$$

Here $n_0 = \rho_0 d$ is the average number of particles per site, where d is the lattice spacing. Power-law behavior is also observed in a variety of other correlation functions, such as the density-density correlation function. The exponents depend on the Luttinger parameter K and in that sense they are tunable functions of the number density and interaction strength. As the Luttinger parameter determines the long-distance behavior of the correlation functions, its value also determines the propensity of the system to order in different ways. The single-component 1D Bose-Hubbard model hosts two phases: a Mott insulating phase and a superfluid (Luttinger-liquid) phase. In the superfluid (SF) phase $K < 1$, while at the SF-Mott transition $K \rightarrow 1$; the only exception is at the Mott lobe tip, where the SF-Mott transition is in the XY universality class [41] and the system undergoes a BKT transition [34–36] in which $K \rightarrow 1/2$.

III. DEFINING SUPERFLUID DENSITY

One of our goals is to clearly articulate the subtleties arising in 1D superfluids. As prefaced in the Introduction, superfluidity in one dimension is unconventional. Not only is Bose-Einstein condensation absent in these systems, but the very definition of superfluid fraction has ambiguities. We emphasize that this is not merely an issue of theoretical importance: As we show in Sec. III C, this has led to a discrepancy between theory and experiment that necessitates a more nuanced understanding of 1D superfluidity.

It will be useful to have a concrete picture in mind. For the purposes of this section, we will imagine a 1D channel of length L , which forms a ring with radius $R = L/2\pi$. We will consider some artificial magnetic flux threading the ring or equivalently a vector potential that points along the channel. The flux induces a current and the current response defines the superfluid fraction. One can imagine equilibrium and nonequilibrium formulations of this thought experiment [42]. In the former, one inserts a small amount of flux and allows the system to come to its true ground state. If the flux is small enough, the resulting state will carry a finite current whose magnitude is proportional to the flux. This is known as the Hess-Fairbank effect [43]. Fundamentally, it is a mesoscopic effect because the equilibrium current is a periodic function of the flux, and the relevant magnetic fields scale as $1/R$. The nonequilibrium formulation involves first allowing the system to equilibrate in the presence of a large magnetic field. One then turns off the magnetic field. Assuming friction with the walls, a normal fluid rapidly comes to rest. A superfluid will not. Typically, one expects that the superfluid fraction

measured via these two approaches will agree [42]. This is not the case in one dimension.

A. Drude weight, superfluid density, and helicity moduli

One of the subtleties we need to contend with is the formal similarities between a superfluid and an ideal zero-temperature metal. Here we elucidate the issue and give the formal definition of superfluid density in terms of response functions and the helicity modulus. We will use the latter definition throughout the paper.

In the absence of impurities, metals are characterized by a resistivity which falls with temperature. At zero temperature they support dissipationless currents. The distinction from superfluidity is the robustness against adding disorder: Weak disorder does not cause dissipation in a superfluid, but it does in a metal.

In dimensions $d > 1$ superfluids and metals can be distinguished by the properties of the transverse current-current correlation function

$$T_{\alpha\alpha}(\mathbf{q}, i\omega_n) = \frac{1}{N} \int_0^\beta d\tau e^{i\omega_n\tau} \langle j_\alpha(\mathbf{q}, \tau) j_\alpha(-\mathbf{q}, 0) \rangle. \quad (6)$$

Here $\omega_n = 2\pi nT$ are the Matsubara frequencies and $\beta = 1/T$ is the inverse temperature (we henceforth set $k_B = 1$). This is the transverse correlation function when \mathbf{q} is orthogonal to $\hat{\alpha}$. The correlation function at real frequencies is obtained by analytic continuation $i\omega_n \rightarrow \omega + i\delta$. Note that this correlation function cannot be defined in one dimension as there is no transverse direction.

In linear response theory, the current-current correlation function quantifies the amount of current generated by a vector potential (or a fictitious vector potential which appears from moving frames). If we consider fluid flow in a pipe, the longitudinal response is typified by having moving end caps, while the transverse response corresponds to moving an open pipe. In a superfluid, only the normal component will move with the walls and the superfluid density is given by $\rho_s = \pi m^* D_s$, where m^* is the effective mass and [44]

$$D_s = -\langle K_x \rangle - \lim_{q_y \rightarrow 0} T_{xx}(q_y, 0). \quad (7)$$

In the context of a Hubbard model, $\langle K_x \rangle$ is the expectation value of the kinetic energy per site due to motion in the \hat{x} direction. This static response corresponds to the Hess-Fairbank effect previously introduced. Note that $T_{xx}(\mathbf{q}, 0)$ is poorly behaved at $\mathbf{q} = \mathbf{0}$, as the longitudinal $T_{xx}(q_x, 0)$ and transverse $T_{xx}(q_y, 0)$ responses differ.

By taking limits in a different way, one can calculate the Drude weight [44]

$$D = -\langle K_x \rangle - \lim_{\omega \rightarrow 0} T_{xx}(\mathbf{0}, \omega). \quad (8)$$

This corresponds to the response to a homogeneous electric field. Again, the limit is necessary as the point ($q = 0, \omega = 0$) is singular. In a superfluid, both D_s and D are nonzero, in a metal $D_s = 0$ but $D \neq 0$, and in an insulator both D_s and D vanish [44,45]. While Eq. (7) is not well defined in one dimension, Eq. (8) is.

In order to extend the definition of superfluid density to one dimension, it is useful to reformulate the problem in terms of

the helicity modulus [46]. The helicity modulus Υ gives the free-energy response of the system to a twist of the boundary conditions. For example, if the d -dimensional many-body wave function obeys $\Psi(\mathbf{x}) = e^{i\Phi} \Psi(\mathbf{x} + L_\alpha \hat{\alpha})$, then at finite temperature one defines

$$\frac{1}{V} (F[\Phi] - F_0) = \frac{1}{2} \Upsilon \left(\frac{\Phi}{L_\alpha} \right)^2 + \dots, \quad (9)$$

where V is the volume of the system, F is the free energy, and L_α is the length of the system along $\hat{\alpha}$. By the fluctuation dissipation theorem [46], $\Upsilon = \hbar^2 \pi D_s$, and Eq. (9) can be used to define the superfluid density. Unfortunately, the $T \rightarrow 0$ limit and the $L_\alpha \rightarrow \infty$ limits do not commute. If one takes the $T \rightarrow 0$ limit of Eq. (9)

$$\frac{1}{V} (E[\Phi] - E_0) = \frac{1}{2} \Upsilon_0 \left(\frac{\Phi}{L_\alpha} \right)^2 + \dots, \quad (10)$$

then the helicity modulus instead gives the Drude weight $\Upsilon_0 = \hbar^2 \pi D$ [46].

There is no conceptual difficulty in extending the definitions in Eqs. (9) and (10) to one-dimensional systems, so this method succeeds in providing a consistent definition of superfluid density. In terms of the original formulation, Eq. (9) amounts to defining the superfluid density in terms of the $\omega = 0, q \rightarrow 0$ limit of the (scalar) current-current correlation function [47]. If one reverses those limits (setting $q = 0$ and taking the limit $\omega \rightarrow 0$) then one produces the Drude weight. As will be argued below, there is a similar story involving the limits $T \rightarrow 0$ and $L \rightarrow \infty$.

B. Thermodynamic and zero-temperature limits

Comparing Eq. (3) with Eq. (10), the zero-temperature helicity modulus is $\Upsilon_0 = \hbar v_j / \pi$. As first shown by Del Maestro and Affleck [12], one can calculate Υ by summing over states with all possible twists (see Appendix A), finding

$$\frac{\Upsilon(L, T)}{\Upsilon_0} = 1 + \frac{\pi^2 \Upsilon_0}{LT} \frac{\vartheta_3''(0, e^{-2\pi^2 \Upsilon_0 / LT})}{\vartheta_3(0, e^{-2\pi^2 \Upsilon_0 / LT})}, \quad (11)$$

where $\theta_3(z, q)$ is the Jacobi theta function of the third kind. The $T \rightarrow 0$ and $L \rightarrow \infty$ limits do not commute: Υ/Υ_0 approaches 1 as $LT \rightarrow 0$ and approaches 0 as $LT \rightarrow \infty$. Taking the thermodynamic limit prior to $T \rightarrow 0$ results in a formally vanishing superfluid density.

This structure arises from a competition between the thermal energy scale T and the gaps between states in different topological sectors: A many-body state with a 2π phase twist across its length L (which consequently supports finite current) differs in energy from the ground state by $\Delta E_{2\pi} = 2\pi \hbar v_j / L$. When one takes the temperature to zero in a system with finite L , one only occupies states with a fixed winding, resulting in a superfluid response. The opposite limit yields a large ensemble of windings and the system behaves like a normal fluid. Note that this peculiarity is specific to one dimension: One finds $\Delta E_{2\pi} \propto L^{d-2}$ in d spatial dimensions, so the energy gap will be finite in the thermodynamic limit for $d \geq 2$ [48].

In our calculation we explicitly work at $T = 0$, and these considerations are irrelevant: Our procedure correctly yields Υ_0 and hence the superfluid density.

C. Nonequilibrium considerations

The arguments so far have been thermodynamic in nature and assumed thermal equilibrium. The energy barriers separating topologically distinct sectors do not vanish in the thermodynamic limit. Therefore, the time to equilibrate will be exponential in $1/T$, even though the states with different windings have degenerate energies. These long relaxation times must be taken into account in modeling experiments in cold-atom systems [49,50] and ^4He nanopores [51–54]. One approach is to introduce dynamical superfluidity [55–58].

There is a close connection between this dynamical superfluidity and the physics described in Sec. III B. In the equilibrium theory, taking $T = 0$, then the limit $L \rightarrow \infty$ freezes the system into a single current-carrying sector and yields a finite superfluid density, analogous to the dynamical superfluid density. The opposite limit yields no phase stiffness. The theory of dynamical superfluid density generalizes this argument to predict the temperature-dependent response of the experimental system.

While this nonequilibrium physics can be very important, we will simply focus on equilibrium superfluidity at zero temperature.

IV. METHODS

We compute the ground-state phase diagram of the 1D Bose-Hubbard model using two infinite tensor network algorithms: iDMRG [5–7] and VUMPS [8,9]. We make use of the ITENSOR library [59] in our implementations. In this section we discuss the relevant features of these techniques as well as our approach to computing the superfluid density. We provide a detailed discussion of the VUMPS algorithm in Appendix B.

Both iDMRG and VUMPS are variational techniques that make use of a matrix product state ansatz: As a basis for the many-body state one considers states with a fixed number of bosons on each site $\{n_j\}$; in the thermodynamic limit j runs from $-\infty$ to ∞ . The wave function in this basis is written as a product of matrices

$$\psi(\dots, n_1, n_2, \dots) = \sum_{\{s\}} \dots A_{s_0 s_1}^{n_1} B_{s_1 s_2}^{n_2} C_{s_2 s_3}^{n_3} \dots, \quad (12)$$

where the sum over $\{s\}$ represents all possible values of the bond indices s_j . The number of values that each s_j takes on is referred to as the bond dimension χ . Describing states with more entanglement requires larger χ . An arbitrary state can be written in this form if the bond dimension is sufficiently large. Both iDMRG and VUMPS find the lowest-energy matrix product state (MPS) with some enforced constraints on the bond dimension. They principally differ in how they carry out the minimization.

The iDMRG algorithm begins by choosing an initial two-site MPS. For example, one could start with the exact ground

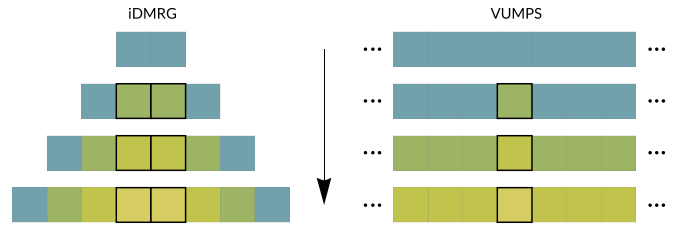


FIG. 1. Schematic showing the difference between the iDMRG and VUMPS algorithms. Blocks denote a matrix product state composed of the contraction of single-site tensors. In each iteration, the state from the previous iteration serves as a bath from which the next optimal state is chosen. While iDMRG grows a finite chain outward, VUMPS performs global updates after each iteration and enforces that the state be translationally invariant.

state of the two-site problem written as an MPS: $\psi_0(n_1, n_2) = \sum_s A_s^{n_1} Z_s^{n_2}$. In Fig. 1 this initial state is depicted as two boxes, representing \mathbf{A} and \mathbf{Z} . After truncating the bond dimension and appropriately normalizing the matrices, one appends two sites to the center of the chain, finding matrices \mathbf{B} and \mathbf{Y} which minimize the energy of the four-site problem with $\psi_1(n_1, n_2, n_3, n_4) = \sum_{\{s\}} \bar{A}_{s_1}^{n_1} B_{s_1 s_2}^{n_2} Y_{s_2 s_3}^{n_3} \bar{Z}_{s_3}^{n_4}$. Here $\bar{\mathbf{A}}$ and $\bar{\mathbf{Z}}$ are the transformed versions of \mathbf{A} and \mathbf{Z} and are held fixed during the optimization with respect to \mathbf{B} and \mathbf{Y} [2]. As depicted in the figure, this procedure is iterated until the matrices added to the center in successive iterations are sufficiently similar. One then approximates the translationally invariant ground state of the Hamiltonian as an infinite chain composed of those matrices.

The iterative growth procedure of iDMRG can be compared to VUMPS, where, as illustrated in Fig. 1, a single site is inserted in the middle of an infinite matrix product state. One finds the tensor for that site that minimizes the energy and then constructs an infinite product state from it. As we will discuss in more detail in Sec. V, this global update is particularly useful when the ground state has long-range correlations and allows one to overcome some of the bottlenecks present in the iDMRG algorithm’s local updates.

There are some additional technical differences between our implementations of iDMRG and VUMPS which are related to single-site vs two-site updating. In a single-site update procedure one finds a true variational minimum at fixed bond dimension, while in a two-site approach there is a truncation error associated with decomposing the two sites [8,10]. Conversely, the two-site procedure samples a larger variational subspace and more readily allows for dynamically changing the bond dimension. Although we do not report the results here, we also implemented a two-site VUMPS algorithm. We found that the truncation error interacted poorly with the procedure of constructing the infinite matrix product state, resulting in less accurate results for the same bond dimension.

Calculating ρ_s

We calculate the superfluid density by first applying a gauge transformation $U a_j U^\dagger = e^{-i\varphi_j} a_j$ to the terms in the Hamiltonian. We then construct the lowest-energy uniform matrix product state. This results in a current carrying state and is analogous to having twisted boundary conditions [60].

The helicity modulus is extracted from the energy as a function of φ according to Eq. (10). The superfluid density is then $\rho_s = \Upsilon_0/2t$, where t is the hopping matrix element in Eq. (1).

We emphasize that this procedure is not the same as simply applying a gauge transformation to the ground-state wave function. The gauge transformation is not homogeneous and hence converts a uniform matrix product state to a nonuniform one. The tensors in our wave function can be used to make a length L matrix product state on a ring with a phase twist $\Phi = L\varphi$ across the boundary.

V. RESULTS

As reviewed in Sec. II, the Luttinger-liquid phase is critical, with an infinite correlation length and power-law decaying correlation functions [see Eq. (5)]. Consequently, the entanglement entropy diverges. An MPS with finite bond dimension will be an approximant, with finite entanglement entropy. The critical structure can be revealed by studying how various quantities scale with bond dimension. Such finite entanglement scaling [61] is closely related to finite-size scaling, where the bond dimension is viewed as a control parameter which adjusts a spatial cutoff [62].

Local quantities (energy, short-range correlations, etc.) converge rapidly with bond dimension. Long-range properties are readily found using scaling analysis. As described below, one sees excellent scaling collapse with moderate bond dimensions: $\chi \sim 20\text{--}50$.

In Sec. VA we show the behavior of the single-particle density matrix and define the correlation length. We also compare the convergence properties of iDMRG and VUMPS in the superfluid phase, attributing the superiority of the latter to finite-size effects in the iDMRG algorithm. In Sec. VB we discuss the properties of the momentum distribution and demonstrate finite entanglement scaling via a scaling collapse. In Sec. VC we plot the superfluid density across the phase diagram and discuss its relationship to the single-particle density matrix. We also determine the Luttinger parameter K as a function of μ/U and t/U . In Sec. VD we conclude by discussing how the entanglement of the MPS ansatz scales with bond dimension, extracting the conformal exponent κ predicted in Ref. [62].

A. Density matrix: iDMRG and VUMPS

Figure 2 shows the single-particle density matrix $\langle a_i a_j^\dagger \rangle$ as a function of spatial separation $|i - j|$ for a representative point in the superfluid phase, $(t/U, \mu/U) = (0.2, 0.5)$. The expected Luttinger-liquid algebraic decay is seen over a wide range of separations. The finite bond dimension introduces an artificial cutoff beyond which $\langle a_i a_j^\dagger \rangle$ is constant. It is natural to define a bond-dimension-dependent quasicondensate density

$$\lim_{|i-j| \rightarrow \infty} \langle a_i a_j^\dagger \rangle \rightarrow |\langle a_i \rangle|^2 \equiv \rho_{\text{qc}}. \quad (13)$$

The fact that there is no Bose-Einstein condensation in one dimension is manifest in the fact that $\rho_{\text{qc}} \rightarrow 0$ as $\chi \rightarrow \infty$.

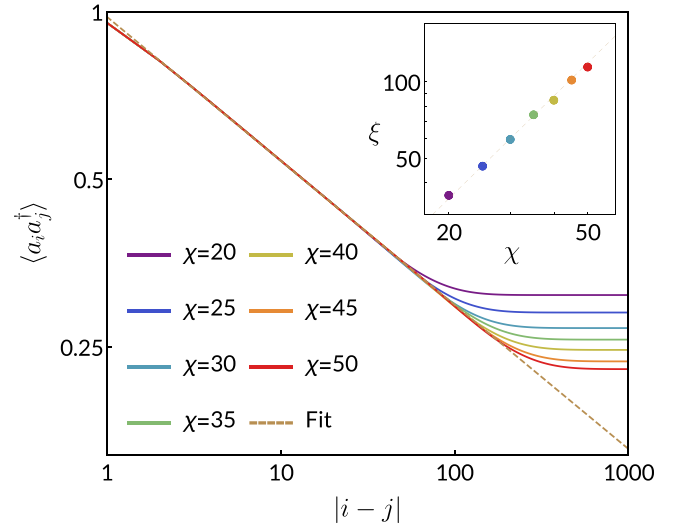


FIG. 2. A log-log plot of the density matrix $\langle a_i a_j^\dagger \rangle$ versus spatial separation $|i - j|$ for a variety of bond dimensions. Data are taken at the point $(t/U, \mu/U) = (0.2, 0.5)$. The Luttinger parameter is extracted from the slope of the power-law region (dashed line). The inset shows a plot of the correlation length $\xi(\chi)$, computed using Eq. (14), versus bond dimension on a log-log scale. Also shown is a fit (dashed line) of the form $\xi(\chi) = \alpha \chi^\kappa$, with $\kappa = 6/(1 + \sqrt{12})$ and α a free parameter.

The correlation length, defined by

$$\xi^2(\chi) = \left(\sum_j j^2 \langle a_0 a_j^\dagger \rangle_c \right) / \left(\sum_j \langle a_0 a_j^\dagger \rangle_c \right), \quad (14)$$

is shown in the inset of Fig. 2. Here $\langle a_0 a_j^\dagger \rangle_c = \langle a_0 a_j^\dagger \rangle - \rho_{\text{qc}}$. The correlation length grows as a power law $\xi(\chi) \propto \chi^\kappa$, where $\kappa = 6/(1 + \sqrt{12})$, as expected from the conformal invariance of the Luttinger liquid [61,62].

This correlation length can be viewed as a spatial cutoff, and the quasicondensate in this model is very similar to quasicondensates found in finite-length systems [63]. In Appendix C we show that $\rho_{\text{qc}} \sim \xi^{-K/2}$, which is similar to the finite-size scaling $\rho_{\text{qc}} \sim L^{-K/2}$ in Refs. [64–66].

These properties of the single-particle density matrix shed light on the convergence properties of iDMRG and VUMPS. In Fig. 3(a) we plot the quasicondensate density ρ_{qc} versus iteration number for a single run of VUMPS (solid lines) and iDMRG (dashed lines) at various bond dimensions. The quasicondensate density falls with the iteration number, eventually converging to a bond-dimension-dependent constant. Finite truncation error in the two-site state updates in the iDMRG algorithm limit its accuracy, leading to a slightly different value of ρ_{qc} compared to VUMPS. The one-site state updates used by VUMPS work at fixed bond dimension and hence do not introduce any truncation error. In addition to being more accurate, VUMPS converges in many fewer iterations than iDMRG. For $\chi = 40$, a single iteration of VUMPS takes roughly twice as much computer time as a single iteration of iDMRG and is therefore more efficient.

In Fig. 3(b) we show the spatial dependence of the converged density matrix $\langle a_i a_j^\dagger \rangle$. That correlation function, with $|i - j| = n$, is remarkably similar to the long-range

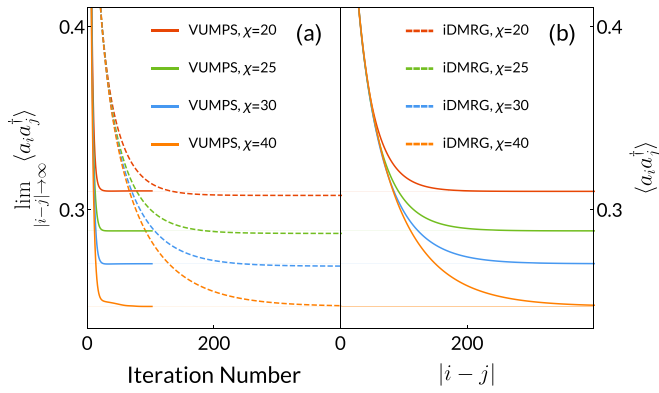


FIG. 3. (a) Plot of the quasicondensate density $\lim_{|i-j| \rightarrow \infty} \langle a_i a_j^\dagger \rangle$ versus iteration number for a single run of VUMPS (solid lines) and iDMRG (dashed lines). Results are plotted for various bond dimensions at the point $(t/U, \mu/U) = (0.2, 0.5)$. Convergence can be understood when the curves saturate at the asymptotic limits (translucent lines). Clearly VUMPS converges in fewer iterations than iDMRG. The discrepancy between the asymptotic limits is due to the truncation error inherent in the two-site iDMRG algorithm; the one-site updates in VUMPS, by contrast, converge to the variational minimum. (b) Plot of the density matrix $\langle a_i a_j^\dagger \rangle$ versus spatial separation $|i-j|$. Results are from fully converged states, computed with VUMPS, at the same point in parameter space. The decay of the density matrix with distance quantitatively mirrors the decrease in the quasicondensate density with iteration number in the iDMRG algorithm.

correlations $\rho_{qc} = \lim_{|i-j| \rightarrow \infty} \langle a_i a_j^\dagger \rangle$ of the n th iteration of the iDMRG algorithm. This structure is understood by noting that after n iterations, iDMRG describes a system of length $2n$. When $n < \xi$, this finite size introduces a cutoff. One consequence is that the number of iterations required for iDMRG convergence grows at least as fast as $\xi \propto \chi^k$. VUMPS does not suffer this problem and has better scaling

with χ . This benefit should be found in any critical or gapless phase/point.

B. Momentum distribution

The noncondensed momentum distribution function $\langle n_k \rangle$ is easily obtained as the Fourier transform of the density matrix

$$\langle n_k \rangle = \sum_j e^{ikj} \langle a_0 a_j^\dagger \rangle_c, \quad (15)$$

where, as before, $\langle a_0 a_j^\dagger \rangle_c = \langle a_0 a_j^\dagger \rangle - \rho_{qc}$. We plot $\langle n_k \rangle$ versus k for a variety of bond dimensions at $(t/U, \mu/U) = (0.2, 0.5)$ in Fig. 4(a). The momentum distribution function is sharply peaked about $k = 0$. This is not a signature of Bose-Einstein condensation, but is instead indicative of the critical scaling of the density matrix. At long distances the density matrix falls off as $r^{-K/2}$; by power-law counting its Fourier transform scales as $k^{K/2-1}$ for small momenta. As seen in the figure, this small- k divergence is cut off by the finite correlation length in our matrix product state ansatz. The correlation length grows with bond dimension and the momentum distribution function approaches a power law as $\chi \rightarrow \infty$. For $k \gtrsim 0.1$, n_k is independent of χ . This is equivalent to the collapse in Fig. 2 and indicates that the short-distance correlations are well captured by an MPS with moderate bond dimension. In Fig. 4(b) we demonstrate a scaling collapse by rescaling the momentum and the distribution function by powers of the correlation length $\xi(\chi)$ computed with Eq. (14). The asymptotic power-law behavior, indicated by the dashed line, is visible for $k\xi \sim 10$. Around $k\xi \sim 1$, that divergence is smoothly cut off and all curves approach a constant.

C. Superfluid density

As discussed in the Introduction, unlike in a Galilean-invariant system, the zero-temperature superfluid fraction of the 1D Bose-Hubbard model continuously interpolates

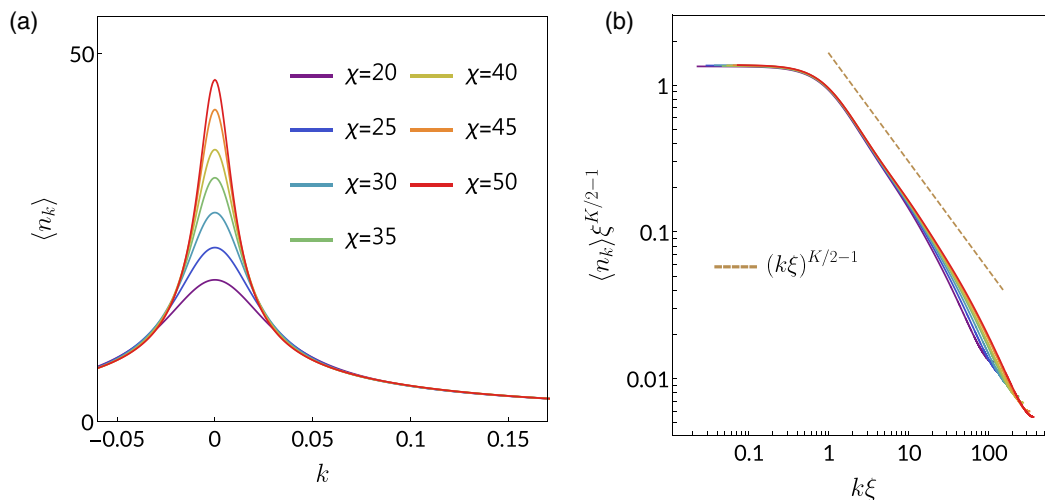


FIG. 4. (a) Plot of the momentum distribution $\langle n_k \rangle$ at the point $(t/U, \mu/U) = (0.2, 0.5)$ for various bond dimensions. The divergence at $k = 0$ is smoothly cut off at fixed bond dimension due to the finite correlation length. Note the curves are almost identical for $|k| > 0.1$ in units of the reciprocal lattice constant. (b) Plot of the momentum distribution functions on a log-log scale after rescaling by powers of the correlation length. Note that the Luttinger parameter K was determined from a fit to the single-particle density matrix (see Fig. 2). This captures the critical behavior for small momenta.

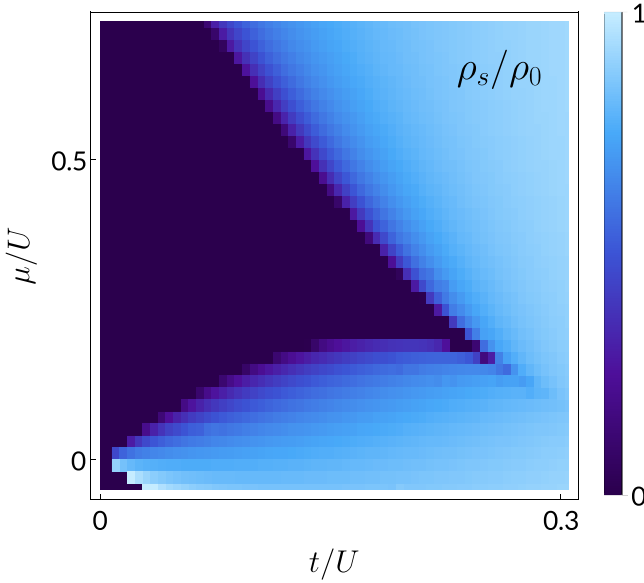


FIG. 5. Superfluid fraction ρ_s/ρ_0 as a function of t/U and μ/U with $\chi = 25$. For $\mu > 0$, the dark region (indicating $\rho_s \rightarrow 0$) is the $n = 1$ Mott lobe. For $\mu < 0$, the dark region indicates the vacuum ($n = 0$).

between 0 and 1. We plot the superfluid fraction ρ_s/ρ_0 with bond dimension $\chi = 25$ as a function of t/U and μ/U in Fig. 5. The $n = 1$ Mott lobe is clearly visible as the dark region where the superfluid fraction vanishes. For $\mu < 0$, the dark region indicates the vacuum. The VUMPS algorithm works directly in the thermodynamic limit and correctly captures the critical behavior away from the tip of the Mott lobe. At the tip the transition is BKT-like, with an expected universal jump in the superfluid density [34–36]. This jump is rounded over at finite χ . Scaling analysis, however, can be used to locate the phase boundary.

The superfluid density can be used to extract the Luttinger parameter: ρ_s is proportional to the characteristic velocity of phase fluctuations, $v_j = u/K$ (see Secs. II and IV). To extract K , one needs to also calculate the charge compressibility $\kappa = \partial n/\partial \mu = 1/\hbar\pi v_n$ [40], where $v_n = uK$ is the characteristic velocity of density fluctuations. In Fig. 6 we compute the Luttinger parameter across the zero-temperature phase diagram, approximating the compressibility using a discrete derivative of the density. The accuracy of this technique and associated error bars are discussed in Appendix D. In the superfluid phase, $K \leq 1$ due to the short-range nature of the Hubbard interactions [21,40]. The Luttinger parameter approaches 1 at the density-driven Mott transition. By contrast, one expects $K \rightarrow 1/2$ at the Mott lobe tip, where the transition is BKT-like. In Fig. 6 we identify the contour along which $K = 1/2$ with dots. Blue dots denote the points on the contour for which the particle density $n > 1$ and red dots denote the points where $n < 1$. We extrapolate to find the intersection of the $n > 1$ branch with the contour of unit density ($n = 1$) to approximate the position of the BKT transition. We find $t_c/U \approx 0.29$, which is in good agreement with previous numerical investigations [67]. We expect t_c to be pushed to larger values as the bond dimension is increased [25]. As with other

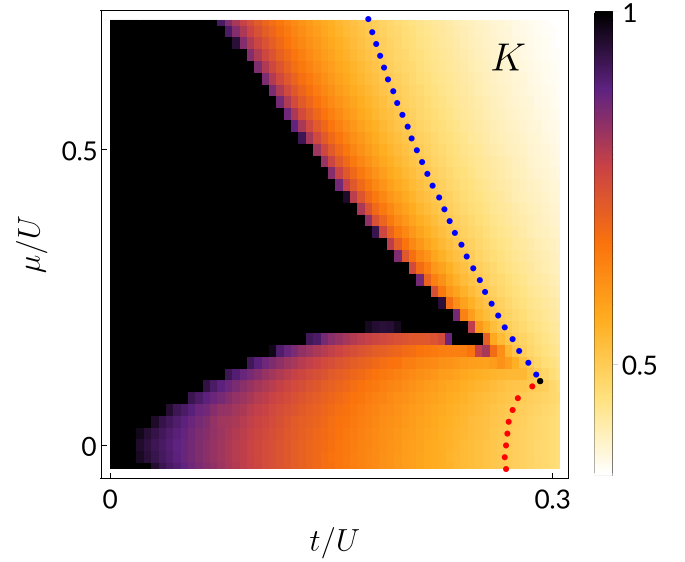


FIG. 6. Luttinger parameter K as a function of t/U and μ/U with $\chi = 25$. In the superfluid phase, $0 < K < 1$; at the density-driven Mott-SF transition, $K \rightarrow 1$. The Mott lobe tip, where $K \rightarrow 1/2$, is obscured due to finite-correlation-length effects. We denote the points where $K = 1/2$ with dots: Blue dots give the points for which $n > 1$, red dots give the points for $n < 1$, and the black dot is an extrapolation to find the Mott lobe tip, where $n = 1$.

features of the BKT transition, scaling arguments are required to extract the precise location of the transition point.

At the base of the Mott lobe ($t, \mu \rightarrow 0$), the Luttinger parameter is well behaved while the superfluid density (as seen in Fig. 5) rapidly changes as a function of μ/U . In particular, the limit $(t/U, \mu/U) \rightarrow (0, 0)$ is singular, with the superfluid fraction taking on any value between 0 and 1 depending on the ratio μ/t . In the vicinity of the vacuum line ($\mu \rightarrow -2t$), the density is small and the effects of the lattice can be ignored. Thus, as expected for a translationally invariant system, the superfluid fraction approaches unity [1]. Conversely, at the Mott transition ($\mu \rightarrow 2t$ for small t/U) the superfluid density vanishes. One can interpret the point $(t/U, \mu/U) = (0, 0)$ as the hard-core limit $U \rightarrow \infty$. This lattice analog of the Tonks-Girardeau gas [68] maps directly onto noninteracting fermions [69]. Figure 6 shows that $K \rightarrow 1$ in this limit, as one expects for noninteracting fermions. Using the relationship between the zero-temperature superfluid density and the Drude weight [see Eq. (11)], one finds that the superfluid density in the hard-core limit is given by [67]

$$\rho_s^{\text{HC}}(\rho_0) = \frac{\sin(\pi \rho_0 d)}{\pi d}, \quad (16)$$

where d is the lattice spacing and the particle density ρ_0 is identical to that of a noninteracting fermions in one dimension,

$$\rho_0\left(\frac{\mu}{t}\right) = \frac{1}{\pi d} \arccos\left(-\frac{\mu}{2t}\right). \quad (17)$$

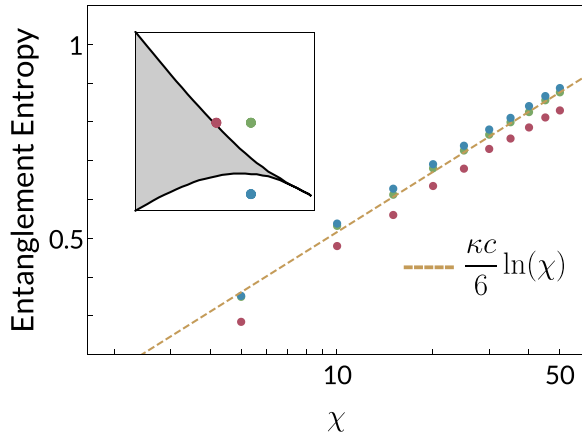


FIG. 7. Plot of the entanglement entropy between bipartitions of the infinite system versus bond dimension on a semilogarithmic scale. Colored dots in the inset show the points on the $t/U - \mu/U$ phase diagram where data were taken. Horizontal and vertical ranges of the inset's axes roughly correspond to those of Figs. 5 and 6. We observe the expected logarithmic scaling of the entropy with bond dimension. The dashed line shows the expected scaling of the entanglement entropy based on the calculation in Ref. [62]. We find excellent agreement with this prediction.

D. Entanglement

As described in Sec. II, the Luttinger-liquid phase of the 1D Bose-Hubbard model is a gapless critical phase. As such, the entanglement entropy between a region of length L and the rest of the system scales as $S = (c/6) \log(L)$, where c is the conformal charge [70]. For a Luttinger liquid, $c = 1$. In the thermodynamic limit the entanglement entropy should diverge; at finite bond dimension χ , however, our matrix product state has a finite correlation length ξ that cuts off the entanglement. One therefore expects that for large ξ [61,62],

$$S(\chi) = \frac{c}{6} \ln[\xi(\chi)] \quad (18)$$

$$\sim \frac{\kappa c}{6} \ln(\chi), \quad (19)$$

where we have used the relation $\xi \sim \chi^\kappa$ with

$$\kappa = \frac{6}{c(\sqrt{12/c} + 1)}. \quad (20)$$

In Fig. 7 we plot the entanglement entropy versus bond dimension on a semilogarithmic plot at a few representative points in the Luttinger-liquid phase. We find good agreement with the prediction in Eqs. (19) and (20). Furthermore, the scaling of the correlation length agrees with that shown in the inset of Fig. 2, which is determined entirely from the correlation function $\langle a_i a_j^\dagger \rangle$.

VI. EXPERIMENTAL APPLICATIONS

As described in Sec. II, the superfluid density is a natural observable in bulk superfluid helium. Measuring the superfluid density in a 1D lattice system, however, is more challenging. The two most promising settings are helium or ultracold atoms. In fact, one-dimensional superfluidity has been studied using ^4He adsorbed in channels a few

nanometers in diameter [52]. The 1D regime is reached when the thermal wavelength of the ^4He is large compared to the diameter of the tubes. This condition can be understood as the freezing out of transverse modes, which are gapped due to their quantization. The array of 1D tubes is then placed on a torsional oscillator with a sufficiently low frequency of oscillation to only excite longitudinal modes of the nanotubes [51–53]. One can then extract a frequency shift that is directly related to the superfluid density. Unfortunately, in this setting there is no simple way to add a lattice or control the interaction strength.

Cold atoms can overcome both of these issues. The 1D Bose-Hubbard Hamiltonian is the natural description of bosonic atoms in a deep optical lattice. Moreover, the contact interactions can be tuned by a Feshbach resonance [71,72]. Again, the 1D regime is realized by applying sufficiently large transverse confinement, freezing out the transverse modes. Unfortunately, measuring the superfluid density in cold-atom systems is difficult.

In the absence of a lattice, there have been at least four ways to meet this challenge: (i) collective modes, (ii) density response to rotation, (iii) spectral response to an artificial vector potential, and (iv) velocities of first and second sound. We briefly describe each of these. So far all experiments and proposals have been in either three or two dimensions.

Adapting these approaches to a 1D Bose-Hubbard system would require substantial work. Method (i) does not have an obvious analog in one dimension. Methods (ii) and (iii) would require a periodic ring geometry [73], which has not been realized with a lattice. Method (iv) does not apply in one dimension. We briefly elaborate on each of these.

(i) *Collective modes.* The lowest-energy mode of a gas in an anisotropic trap is analogous to the fundamental mode of a torsional oscillator and hence provides information about superfluidity [74–81]. For example, the precession frequency of quadrupole modes has been used to extract the moment of inertia of the unitary Fermi gas [82] and of dipolar bosons [83] in three dimensions. The superfluid fraction can then be determined by the reduction of the moment of inertia from that of a rigid body. This technique relies on a hydrodynamic description of the cloud and hence requires sufficiently strong interactions. One major challenge here is that the trapped system is highly inhomogeneous and the measured superfluid fraction is spatially averaged. Driving the collective modes can also heat the sample or excite vortices. Further, this technique is not directly applicable in the presence of an optical lattice. The lattice breaks rotational symmetry, which complicates the relationship between the frequencies of the quadrupole modes and the superfluid density.

(ii) *Density response to rotation.* Ho and Zhou argued that the local superfluid density in three dimensions can be extracted from the response of the column density profile to rotation [84]. Importantly, their approach directly gives the spatial dependence of the superfluid density in an inhomogeneous trap. The derivation, however, relies on a strictly harmonic trapping potential and would need to be modified to include a lattice.

(iii) *Spectral response to an artificial vector potential.* Rather than stirring a trapped gas with a potential deformation [82,83], one can probe superfluidity by introducing

a Raman-induced artificial vector potential [85,86]: A set of Raman lasers dresses the atomic states in such a way that they experience an artificial magnetic field. Cooper and Hadzibabic [87,88] showed that the superfluid density can be determined from the populations of the Raman-dressed bands. This enables a spectroscopic determination of superfluid density which can potentially be spatially resolved [89].

(iv) *Velocities of first and second sound.* Experiments by Sidorenkov *et al.* [90] and Christodoulou *et al.* [91] determined the superfluid density in 2D systems by measuring the velocities of the first and second sounds. Similar sound-speed measurements can be carried out in lattice gases. Unfortunately, the two-fluid hydrodynamics of a Luttinger liquid differs from that of higher-dimensional superfluids [92–95]. Specifically, in dimension d , as $T \rightarrow 0$ the ratio of the velocities' first and second sound modes approaches \sqrt{d} . As these modes travel at the same velocity in one dimension, they do not fully decouple, invalidating the analysis that was used to find the superfluid density of the 2D systems.

One important feature of all of these experiments (both cold atoms and ^4He) is that they occur in a system of finite size and at a finite temperature. Furthermore, as discussed in Sec. III C, care must be taken to observe equilibrium properties. Turning these challenges around, one could explore features such as the scaling of the superfluid density with size and temperature, as described by Eq. (11). In particular, the scaled superfluid density is a universal function of the dimensionless parameter

$$x = \frac{Lk_B T}{2ta^2 \rho_s} = \frac{l k_B T}{2tn_s}, \quad (21)$$

where a is the lattice spacing, $l = L/a$ is the number of lattice sites, and $n_s = a\rho_s$ is the zero-temperature superfluid number density. Modern ultracold-atom experiments can realize optical lattices of $O(100)$ sites and temperatures down to ~ 0.1 times the bandwidth, which in this case is $4t$. Hence, by tuning the temperature and lattice size, contemporary experiments could study the scaling function in regions where the dimensionless parameter takes on values $1 \lesssim x \lesssim 100$. Note that the lower bound is more stringent, arising due to limitations in preparing low-temperature systems and lower bounds on the number of particles necessary to see Luttinger-liquid-like phenomenology [here we posit that $O(10)$ sites are necessary]. These values for the dimensionless scaling parameter are comparable to those realized in recent experiments on ^4He nanotubes [51–54].

VII. SUMMARY

We have provided a comprehensive discussion of superfluidity in the 1D Bose-Hubbard model, aided by numerical simulations with infinite matrix product state techniques. The zero-temperature superfluid fraction is related to a Drude weight, which we measure directly from the response to a phase twist. We discuss both finite-temperature and finite-size considerations and how they depend on dimension.

Our work demonstrates the success of using infinite matrix product state techniques to model gapless critical systems. We illustrate a specific advantage of VUMPS over iDMRG in such systems, namely, the ability to efficiently capture

long-range correlations and entanglement even after a small number of iterations.

In addition to calculating superfluid densities, we use several independent approaches to extract the Luttinger parameters which parametrize all long-wavelength properties of the gas. These disparate approaches show nontrivial behavior and agree with one another. Furthermore, we explore connections between finite-size scaling and finite-entanglement scaling.

ACKNOWLEDGMENTS

We thank Jim Sethna, Joel Moore, and Matt Fishman for helpful conversations. This material is based upon work supported by the National Science Foundation under Grant No. PHY-2110250.

APPENDIX A: HELICITY MODULUS OF A LUTTINGER LIQUID

The helicity modulus $\Upsilon(L, T)$ of a 1D system of length L and temperature T is defined as

$$\frac{F[L, T, \Phi] - F_0[L, T]}{L} = \frac{1}{2} \Upsilon(L, T) \left(\frac{\Phi}{L} \right)^2 + \dots, \quad (\text{A1})$$

where F is the free energy and Φ is the phase twist across the periodic boundaries $\Psi(x+L) = e^{i\Phi} \Psi(x)$. The omitted terms scale as $(\Phi/L)^4$. As reported in [12], this quantity can be exactly calculated for a Luttinger liquid, described by a Hamiltonian

$$\frac{\mathcal{H}_{\text{LL}}}{\hbar} = \sum_{q \neq 0} \omega_q b_q^\dagger b_q + \left(\frac{\pi}{2L} \right) [v_j J^2 + v_n (N - N_0)^2].$$

As described in Sec. II, J is the winding number, N is the number of bosons, and b_q are excitations of momentum q . Here we present an explicit derivation of the resulting helicity modulus.

We begin by noting that the partition function $Z = \exp(-\beta F)$ factors into the product $Z_b Z_J Z_N$, corresponding to contributions from each term in the Hamiltonian. Of these, only the topological phase twist term will be affected by the boundary condition twist. The twist is incorporated by requiring $J = 2j - \Phi/\pi$, where j is an integer, giving us

$$Z_J(\Phi) = \sum_{j=-\infty}^{\infty} \exp\left(-\beta \frac{2\pi v_j}{L} (j + \Phi/2\pi)^2\right) \quad (\text{A2})$$

$$= \sqrt{\frac{LT}{2\pi \Upsilon_0}} \vartheta_3(\Phi/2, e^{-LT/2\Upsilon_0}), \quad (\text{A3})$$

where $\vartheta_3(z, q) = \sum_{n=-\infty}^{\infty} q^{n^2} e^{2niz}$ is the Jacobi theta function of the third kind and $\Upsilon_0 = \hbar v_j/\pi$ is the zero-temperature helicity modulus.

We now Taylor expand the ratio of theta functions for small twist angles, finding

$$\ln \left(\frac{Z_J(\Phi)}{Z_J(0)} \right) = \frac{1}{8} \frac{\vartheta_3''(0, e^{-LT/2\Upsilon_0})}{\vartheta_3(0, e^{-LT/2\Upsilon_0})} \Phi^2 + O(\Phi)^4, \quad (\text{A4})$$

where $\vartheta_3''(z, q) = \partial_z^2 \vartheta_3(z, q)$. Finally, by substituting Eq. (A4) back into Eq. (A1), we obtain an expression for the helicity

modulus:

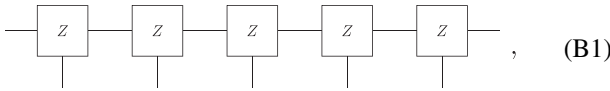
$$\begin{aligned} \frac{\Upsilon(L, T)}{\Upsilon_0} &= -\frac{LT}{4\Upsilon_0} \frac{\vartheta_3''(0, e^{-LT/2\Upsilon_0})}{\vartheta_3(0, e^{-LT/2\Upsilon_0})} \\ &= 1 + \frac{\pi^2 \Upsilon_0}{LT} \frac{\vartheta_3''(0, e^{-2\pi^2 \Upsilon_0/LT})}{\vartheta_3(0, e^{-2\pi^2 \Upsilon_0/LT})}. \end{aligned} \quad (\text{A5})$$

The normalized helicity modulus Υ/Υ_0 is a scaling function that depends only on the quantity LT/Υ_0 . The two forms shown in Eq. (A5), both of which appear in the literature, are related by completing the square. The physical consequences of this result are discussed in Sec. III B.

APPENDIX B: VUMPS IMPLEMENTATION

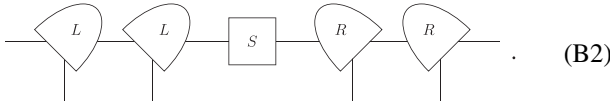
Here we discuss our implementation of the VUMPS algorithm. We refer the reader to Refs. [8,9] for further details and justification. We will follow the standard graphical notation for tensor networks [2]. Throughout this section, graphical equations will show a finite portion of (what should be assumed to be) an infinitely long MPS.

In a given iteration, we begin with a uniform matrix product state. Rather than parametrizing the MPS in the uniform gauge,



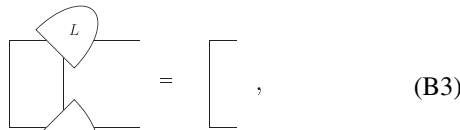
$$, \quad (\text{B1})$$

where the same tensor acts on each site, it is convenient to write the state in mixed-canonical form

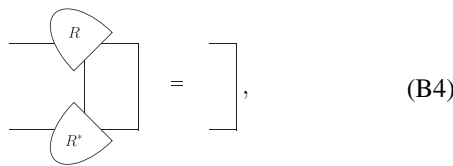


$$. \quad (\text{B2})$$

The uniform and mixed-canonical forms are related by a gauge transformation [2]. The mixed-canonical form is defined by three tensors \mathbf{L} , \mathbf{S} , and \mathbf{R} . As indicated by the shape of their symbols, the tensors \mathbf{L} and \mathbf{R} are left and right orthogonal tensors, obeying



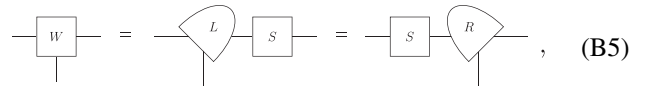
$$, \quad (\text{B3})$$



$$, \quad (\text{B4})$$

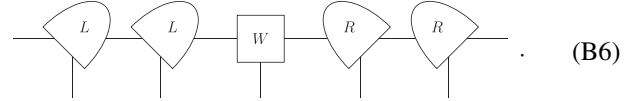
where the symbols on the right-hand side represent identity tensors. This orthogonality dramatically simplifies the calculation of expectation values and hence is the preferred way of storing and manipulating a matrix product state. In order for the state to be translationally invariant, these tensors should

satisfy



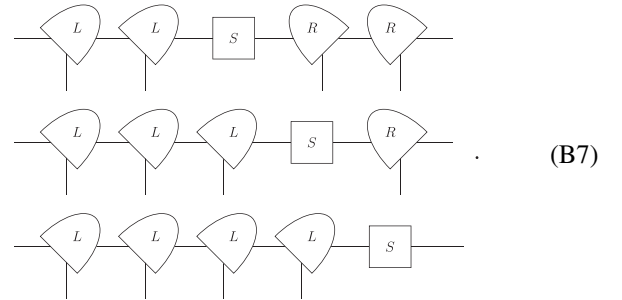
$$, \quad (\text{B5})$$

which defines the tensor \mathbf{W} . The mixed-canonical form can also be written as



$$. \quad (\text{B6})$$

Graphically, Eq. (B5) implies that one can freely shift the inversion center of the uniform MPS without changing any observable properties of the state:

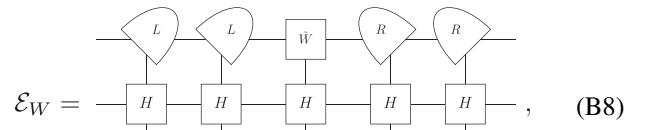


$$. \quad (\text{B7})$$

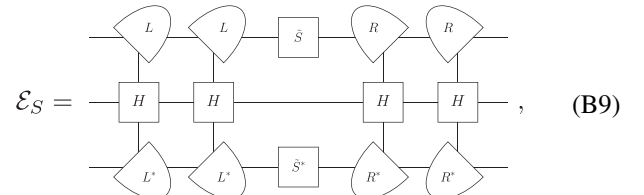
All three of the above states represent the same physical wave function.

A uniform matrix product state is defined by the set of tensors \mathbf{L} , \mathbf{R} , \mathbf{W} , and \mathbf{S} , obeying the constraint in Eq. (B5). The VUMPS algorithm involves using energetic arguments to update \mathbf{W} and \mathbf{S} and linear algebra techniques to update \mathbf{L} and \mathbf{R} . It converges to a uniform matrix product state, but as schematically shown in Fig. 1, at intermediate stages the central site differs from the others. We will discuss one step of the algorithm, going from $\{\mathbf{L}, \mathbf{R}, \mathbf{W}, \mathbf{S}\}$ to $\{\tilde{\mathbf{L}}, \tilde{\mathbf{R}}, \tilde{\mathbf{W}}, \tilde{\mathbf{S}}\}$.

We find $\tilde{\mathbf{W}}$ and $\tilde{\mathbf{S}}$ by minimizing the energies



$$, \quad (\text{B8})$$



$$, \quad (\text{B9})$$

which correspond to expectation values of the Hamiltonian. In Eqs. (B8) and (B9) the Hamiltonian is written as a matrix

product operator (MPO) [2]

$$\begin{array}{c}
 \begin{array}{c} n \\ | \\ \boxed{H} \\ | \\ n' \end{array} \\
 = \begin{pmatrix} \mathbb{I} & -te^{i\varphi} \mathbf{A}^\dagger & -te^{-i\varphi} \mathbf{A} & -(\mu + \frac{U}{2})\mathbf{N} + \frac{U}{2}\mathbf{N}^2 \\ 0 & 0 & 0 & \mathbf{A} \\ 0 & 0 & 0 & \mathbf{A}^\dagger \\ 0 & 0 & 0 & \mathbb{I} \end{pmatrix}.
 \end{array} \quad (\text{B10})$$

where the operators \mathbb{I} , \mathbf{A}^\dagger , \mathbf{A} , \mathbf{N} , and \mathbf{N}^2 are represented as matrices in the number occupation basis (n, n') . The rows and columns of the right-hand side of Eq. (B10) correspond to the left and right legs of the tensor \mathbf{H} , respectively. The Peierls phase φ arises from the gauge transformation discussed in Sec. IV and is used to compute the superfluid density. For the state to be normalized we require that $\|\tilde{\mathbf{W}}\|_2 = \|\tilde{\mathbf{S}}\|_2 = 1$. The square of this norm, which is basis independent, equals the sum of the modulus squared of all matrix elements.

The energies \mathcal{E}_W and \mathcal{E}_S are extensive and hence formally infinite. As explained in Appendixes C and D of Ref. [8], these divergences can be subtracted off. We summarize the procedure for doing so below. The optimal $\tilde{\mathbf{W}}$ and $\tilde{\mathbf{S}}$ solve eigenvalue problems

$$\begin{array}{c}
 \begin{array}{c} \boxed{H_L} \\ | \\ \boxed{H - \varepsilon \mathbb{I}} \\ | \\ \boxed{H_R} \end{array} \\
 = \varepsilon_W \left(\begin{array}{c} \boxed{\tilde{W}} \\ | \\ \boxed{H - \varepsilon \mathbb{I}} \\ | \\ \boxed{H_R} \end{array} \right), \quad (\text{B11})
 \end{array}$$

$$\begin{array}{c}
 \begin{array}{c} \boxed{H_L} \\ | \\ \boxed{H - \varepsilon \mathbb{I}} \\ | \\ \boxed{H_R} \end{array} \\
 = \varepsilon_S \left(\begin{array}{c} \boxed{\tilde{S}} \\ | \\ \boxed{H - \varepsilon \mathbb{I}} \\ | \\ \boxed{H_R} \end{array} \right), \quad (\text{B12})
 \end{array}$$

where $\mathbf{H} - \varepsilon \mathbb{I}$ is the Hamiltonian MPO minus the average energy per site ε [which is defined in Eq. (B18)]. This simply requires modifying the on-site term of Eq. (B10) to be $-(\mu + U/2)\mathbf{N} + (U/2)\mathbf{N}^2 - \varepsilon \mathbb{I}$. The tensors \mathbf{H}_L and \mathbf{H}_R consist of all contributions to the left and right of the central tensor in Eq. (B8), with the same subtraction [8]. For convenience, we will refer to the eigenvalue problems in Eq. (B11) and (B12) as $\mathbf{H}_W(\tilde{\mathbf{W}}) = \varepsilon_W \tilde{\mathbf{W}}$ and $\mathbf{H}_S(\tilde{\mathbf{S}}) = \varepsilon_S \tilde{\mathbf{S}}$.

The tensors \mathbf{H}_L and \mathbf{H}_R can be immediately evaluated using Eqs. (B8) and (B10). Just as \mathbf{H} was written as a matrix of matrices in Eq. (B10), \mathbf{H}_L and \mathbf{H}_R can be represented as vectors of matrices. For example, \mathbf{H}_L is given by

$$\left(\begin{array}{c} \left[\begin{array}{c} -te^{i\varphi} \begin{array}{c} L \\ | \\ \boxed{A^\dagger} \\ | \\ L \end{array} \\ -te^{-i\varphi} \begin{array}{c} L \\ | \\ \boxed{A} \\ | \\ L \end{array} \end{array} \right] \Lambda_L \end{array} \right), \quad (\text{B13})$$

where Λ_L encompasses all terms in the Hamiltonian that act on sites to the left of the central site. Before subtracting off

the divergences, these disconnected terms are given by

$$\begin{array}{c}
 \Lambda_L = -te^{i\varphi} \begin{array}{c} \begin{array}{c} L \\ | \\ \boxed{A^\dagger} \\ | \\ L \end{array} \begin{array}{c} L \\ | \\ \boxed{A} \\ | \\ L \end{array} \begin{array}{c} \sum_{n=0}^{\infty} T_L^n \\ | \\ \end{array} \end{array} + h.c. \\
 -(\mu + U/2) \begin{array}{c} \begin{array}{c} L \\ | \\ \boxed{N} \\ | \\ L \end{array} \begin{array}{c} \sum_{n=0}^{\infty} T_L^n \\ | \\ \end{array} \end{array} \\
 + (U/2) \begin{array}{c} \begin{array}{c} L \\ | \\ \boxed{N^2} \\ | \\ L \end{array} \begin{array}{c} \sum_{n=0}^{\infty} T_L^n \\ | \\ \end{array} \end{array} \\
 \equiv \Lambda_L^0 \begin{array}{c} \sum_{n=0}^{\infty} T_L^n \\ | \\ \end{array}, \quad (\text{B14})
 \end{array}$$

which involves the geometric sum $\sum_{n=0}^{\infty} \mathbf{T}_L^n = (\mathbf{1} - \mathbf{T}_L)^{-1}$, where \mathbf{T}_L is the left-canonical transfer matrix:

$$\begin{array}{c} \begin{array}{c} L \\ | \\ \boxed{} \\ | \\ L^* \end{array} \end{array} = \begin{array}{c} \boxed{T_L} \end{array}. \quad (\text{B15})$$

Subtracting off the divergence formally requires replacing

$$\Lambda_L^0 \rightarrow \tilde{\Lambda}_L^0 = \Lambda_L^0 - \varepsilon \left[\begin{array}{c} \boxed{} \\ | \\ \boxed{} \\ | \\ \boxed{} \end{array} \right]. \quad (\text{B16})$$

In Eq. (B14) the divergence can be associated with the fact that the transfer matrix has an eigenvector with eigenvalue 1. This suggests an alternative renormalization, substituting $\mathbf{T}_L \rightarrow \tilde{\mathbf{T}}_L$ with $\tilde{\mathbf{T}}_L = \mathbf{T}_L - |0_L\rangle\langle 0_L|$, where $|0_L\rangle$ and $\langle 0_L|$ are the dominant left and right eigenvectors of \mathbf{T}_L , respectively. When Eq. (B5) is satisfied, these are given by

$$\langle 0_L| = \left[\begin{array}{c} \boxed{} \\ | \\ \boxed{} \\ | \\ \boxed{} \end{array} \right] \quad |0_L\rangle = \begin{array}{c} \boxed{\tilde{S}} \\ | \\ \boxed{\tilde{S}^*} \end{array}. \quad (\text{B17})$$

To show the equivalence of these approaches, we note that the average energy per site is

$$\varepsilon = \Lambda_L^0 |0_L\rangle = \begin{array}{c} \Lambda_L^0 \\ | \\ \boxed{\tilde{S}} \\ | \\ \boxed{\tilde{S}^*} \end{array}. \quad (\text{B18})$$

Hence the identity $\tilde{\Lambda}_L^0 \mathbf{T}_L^n = \Lambda_L^0 \tilde{\mathbf{T}}_L^n$ can be applied to each term in the geometric sum for $n \geq 1$ [see Eq. (B14)]. This construction implies that \mathbf{H}_L and \mathbf{H}_R are the fixed points of the left and right MPO transfer matrices, respectively:

$$\text{Diagram (B19): } H_L \text{ (box) connected to a loop with } L \text{ (diamond) and } H - \epsilon \mathbb{I} \text{ (box). The loop is connected to another } H_L \text{ (box).} \quad (\text{B19})$$

$$\text{Diagram (B20): } H_R \text{ (box) connected to a loop with } R \text{ (diamond) and } H - \epsilon \mathbb{I} \text{ (box). The loop is connected to another } H_R \text{ (box).} \quad (\text{B20})$$

We then find $\tilde{\mathbf{L}}$ and $\tilde{\mathbf{R}}$ by minimizing

$$\epsilon_g^L = \left\| \text{Diagram (B21): } \tilde{W} \text{ (box) connected to } \tilde{L} \text{ (diamond) connected to } \tilde{S} \text{ (box).} \right\|_2, \quad (\text{B21})$$

$$\epsilon_g^R = \left\| \text{Diagram (B22): } \tilde{W} \text{ (box) connected to } \tilde{S} \text{ (box) connected to } \tilde{R} \text{ (diamond).} \right\|_2. \quad (\text{B22})$$

The gauge-fixing error, defined as $\epsilon_g = \max\{\epsilon_g^L, \epsilon_g^R\}$, quantifies the deviation of the mixed-canonical MPS (defined by tensors $\tilde{\mathbf{L}}$, $\tilde{\mathbf{S}}$, and $\tilde{\mathbf{R}}$) from translational invariance. As the VUMPS algorithm is iterated, we find that ϵ_g decreases and eventually approaches machine precision.

The optimization in Eq. (B21) and (B22) can be performed exactly using two singular-value decompositions. We refer the reader to Sec. II C of Ref. [8] for the expression and for an approximation that better handles singular values near machine precision.

If $\epsilon_g = 0$, the distance from the optimal variational ansatz can be quantified by calculating the magnitude of the gradient of the energy with respect to \mathbf{W} , constrained to the manifold of uniform states. As argued in Refs. [8,9], this gradient can be expressed as

$$\text{Diagram (B23): } G \text{ (box) = } H_W(W) \text{ (box) connected to } L \text{ (diamond) connected to } H_S(S) \text{ (box).} \quad (\text{B23})$$

where we defined the tensors \mathbf{H}_W and \mathbf{H}_S after Eqs. (B11) and (B12). The norm of the gradient, $g \equiv \|\mathbf{G}\|_2$, vanishes at the variational minimum. Even when $\epsilon_g \neq 0$, the quantity g has meaning, and we quantify our proximity to the optimal state by the magnitude of g . In practice, the variational energy converges to within machine precision much faster than g . For the purposes of this paper, we define convergence as $g \leq 10^{-14}$.

One of the strengths of VUMPS is that it can make large steps in parameter space. Unfortunately, the algorithm sometimes stalls out or falls into a limit cycle. When this was the case, we were able to reduce g to the desired precision by

applying state updates using the infinite time-dependent variational principle (iTDVP) [9]. The procedure is very similar to VUMPS except that, instead of solving for the lowest-energy eigenvector of \mathbf{H}_W , we update the state by defining $\tilde{\mathbf{W}} = e^{-\tau \mathbf{H}_W}(\mathbf{W})$, where τ is an imaginary time step and \mathbf{H}_W is defined in Eq. (B11). Of course, the normalization condition ($\|\tilde{\mathbf{W}}\|_2 = 1$) must now be enforced by hand. Similarly, we update $\tilde{\mathbf{S}} = e^{-\tau \mathbf{H}_S}(\mathbf{S})$. In the limit $\tau \rightarrow \infty$, iTDVP state updates and VUMPS state updates are equivalent. One can then proceed as we did with VUMPS, defining $\tilde{\mathbf{L}}$ and $\tilde{\mathbf{R}}$ according to Eqs. (B21) and (B22) and computing the gradient using Eq. (B23).

The iTDVP algorithm should reliably converge to the ground state for small τ , although small time steps also mean that more iterations will be required to reach the variational ground state. We deployed iTDVP updates in two ways: (i) When VUMPS updates would not take g below some threshold, most often $g \sim 10^{-11}$, iTDVP updates with $\tau \sim O(1)$ could reduce g below our convergence criterion and (ii) when the algorithm was prone to falling into limit cycles we used iTDVP updates with $\tau \sim O(0.1)$ in between successive VUMPS updates to improve convergence.

APPENDIX C: QUASICONDENSATE DENSITY

While the 1D Bose-Hubbard model has zero condensate density, a consequence of the Mermin-Wagner theorem [3,4], simulations of the model in finite-size systems will observe a finite quasicondensate density $\rho_{\text{qc}} = |\langle a_i \rangle|^2$. Our simulations are performed in the thermodynamic limit but make use of variational wave functions with finite correlation lengths, producing an analogous effect. One can deduce the asymptotic bond-dimension scaling of the quasicondensate density by approximating the density matrix $\langle a_i a_j^\dagger \rangle$ as a piecewise function that decays as $|i - j|^{-K/2}$ for $|i - j| \leq \xi$ and is constant for $|i - j| > \xi$. Making use of Eq. (20), this cartoon yields a quasicondensate density that scales as

$$\rho_{\text{qc}} \propto \langle a_0 a_\xi^\dagger \rangle \propto \chi^{-\kappa K/2}. \quad (\text{C1})$$

In Fig. 8 we plot ρ_{qc} versus bond dimension on a log-log scale. The quasicondensate density decays as a power law, as expected. The solid lines give fits to the data of the form $\rho_{\text{qc}}(\chi) = \alpha \chi^{-\kappa K/2}$, where α is the only free parameter (K is determined from $\langle a_i a_j^\dagger \rangle$; see Appendix D). The quality of the fits are strong confirmation of Eq. (C1).

APPENDIX D: DETERMINING THE LUTTINGER PARAMETER

The Luttinger parameter K characterizes many of the properties of a Luttinger liquid. As such, there are a variety of ways to determine the Luttinger parameter of a uniform MPS. In Fig. 6 we plot K , computed in three different ways, as a function of μ/U . In this Appendix we compare these methods and discuss their reliability.

Data are taken at fixed $t/U = 0.15$ and using the converged uniform MPS at bond dimensions $\chi = 20, 30, \text{ and } 40$.

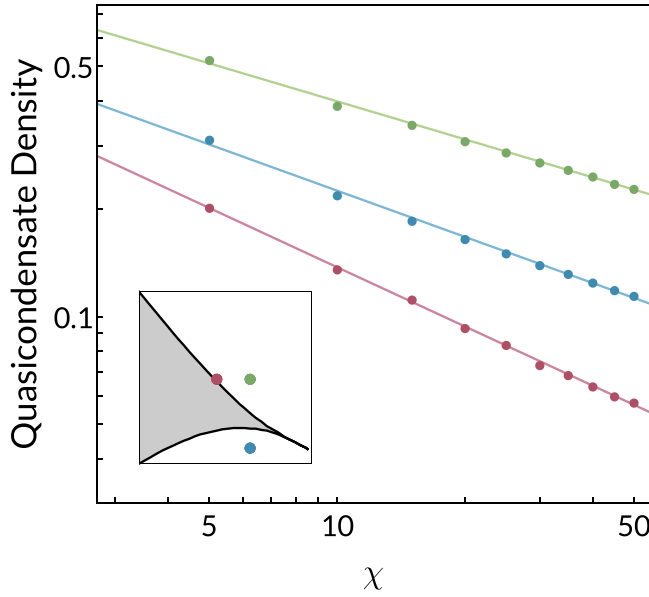


FIG. 8. Quasicondensate density $\rho_{\text{qc}} = |\langle a_i \rangle|^2$ versus bond dimension on a log-log scale for a few representative points in the Luttinger-liquid phase. Solid lines give fits of the form $\rho_{\text{qc}} = \alpha \chi^{-\kappa K/2}$, where α is the only free parameter.

The vertical line at $\mu/U \approx 0.445$ denotes the Mott transition, where $K \rightarrow 1$ [40,41].

The orange curve is determined from $K = \sqrt{v_n/v_j}$, where v_n and v_j are defined in Sec. II. We compute v_j from superfluid density, calculated using the approach in Sec. IV, and the relationship

$$2t\rho_s = \frac{\hbar v_j}{\pi}. \quad (\text{D1})$$

We compute v_n from the compressibility $\kappa = \partial n / \partial \mu$, calculated using finite differences. We measure the density as a function of chemical potential and then apply

$$\kappa = \frac{1}{\hbar\pi v_n}. \quad (\text{D2})$$

Note that this method was also employed in Fig. 6. We establish error bars on the superfluid density by measuring the variance of $\rho_s(\chi)$ at the three different bond dimensions. In general, however, the error bars on the orange curve are dominated by errors in the discrete derivative used to calculate the compressibility.

The blue and green curves in Fig. 9 are both determined from the algebraic decay of the density matrix $\langle a_i a_j^\dagger \rangle$ plotted in Fig. 2. In the blue curve, we take the derivative of $\ln \langle a_i a_j^\dagger \rangle$ with respect to $\ln |i - j|$ and find the average value where the curve plateaus. We establish error bars by taking the standard deviation of the log-derivative over the domain $\ln(|i - j|/\xi) \in (-2, 0)$, where $\xi(\chi)$ is determined by Eq. (14). Note that the power-law behavior breaks down for $|i - j| > \xi$, beyond which $\langle a_i a_j^\dagger \rangle$ decays exponentially to ρ_{qc} .

The green curve is determined by rescaling $\langle a_i a_j^\dagger \rangle$ by a power of the correlation length such that the $\chi = 20, 30$ and

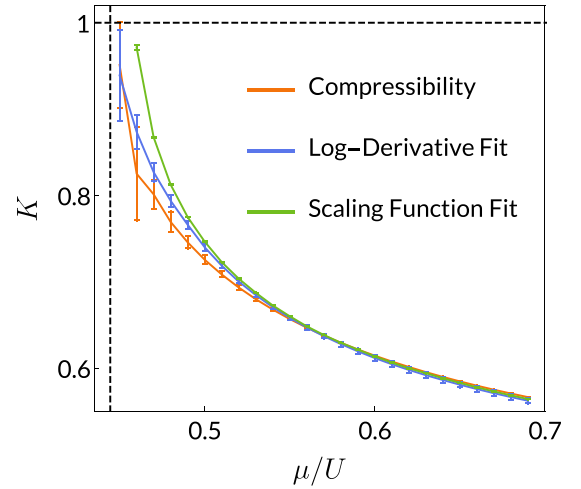


FIG. 9. Plot of the Luttinger parameter versus μ/U at fixed $t/U = 0.15$, determined using three different procedures. The Mott-SF transition point is at $\mu/U \approx 0.445$, denoted by the black dashed line. See Appendix D for an explanation of the procedures.

40 curves exhibit a scaling collapse. The collapsed curves are then fit to a scaling function of the form [96]

$$C(x) = a \left[1 + \left(\frac{x}{b} \right)^{-n\eta} \right]^{1/n} \quad (\text{D3})$$

using a nonlinear least-squares algorithm. In practice, in order to arrive at an unbiased scaling collapse, we exploit the fact that the collapse should occur when we rescale the axes as follows: $|i - j| \rightarrow |i - j|/\xi$ and $\langle a_i a_j^\dagger \rangle \rightarrow \langle a_i a_j^\dagger \rangle \xi^{K/2}$. Furthermore, the parameter η in Eq. (D3) should be equal to $K/2$ at convergence. We therefore implement an iterative scheme to find the optimal value of K : We start by rescaling the curves by an arbitrary power of ξ ; we then fit the data to a scaling function and extract the Luttinger parameter $\tilde{K} = 2\eta$; we then use \tilde{K} to rescale the curves and repeat the process. We need about five iterations to reach convergence. Error bars come from the covariance matrix of the nonlinear least-squares fit, which we then rescale to account for systematic errors in the fitting procedure [97].

We find that the orange and blue curves agree reasonably well within their error bars for all data points. Errors in the orange curve increase near the Mott-SF transition because the curvature of $n(\mu)$ increases, making the discrete derivative approximation less accurate. The error could be improved substantially by taking data at more finely spaced values of μ . As for the blue and green curves, the density matrix develops oscillations that persist to longer and longer distances as one approaches the phase boundary. When this length scale exceeds the correlation length of the uniform MPS it becomes challenging to extract K from $\langle a_i a_j^\dagger \rangle$. In this case, the log-derivative technique (blue curve) yields large error bars that likely encompass the correct value of K . The green curve, on the other hand, systematically overfits based on this behavior and deviates significantly from the other two curves. A second consequence of the overfitting is that the error bars on the

green curve become unreliable near the transition. The accuracy of both the blue and green curves would be substantially

improved by working at larger bond dimensions, where the correlation length is larger.

-
- [1] A. Leggett, *J. Stat. Phys.* **93**, 927 (1998).
- [2] U. Schollwöck, in January 2011 Special Issue, edited by F. Wilczek, special issue of *Ann. Phys. (NY)* **326**, 96 (2011).
- [3] P. C. Hohenberg, *Phys. Rev.* **158**, 383 (1967).
- [4] N. D. Mermin and H. Wagner, *Phys. Rev. Lett.* **17**, 1133 (1966).
- [5] I. P. McCulloch, [arXiv:0804.2509](https://arxiv.org/abs/0804.2509)
- [6] S. R. White, *Phys. Rev. Lett.* **69**, 2863 (1992).
- [7] S. R. White, *Phys. Rev. B* **48**, 10345 (1993).
- [8] V. Zauner-Stauber, L. Vanderstraeten, M. T. Fishman, F. Verstraete, and J. Haegeman, *Phys. Rev. B* **97**, 045145 (2018).
- [9] L. Vanderstraeten, J. Haegeman, and F. Verstraete, *SciPost Phys. Lect. Notes* **7**, 1 (2019).
- [10] S. R. White, *Phys. Rev. B* **72**, 180403(R) (2005).
- [11] L. Vranješ Markić, H. Vrcan, Z. Zuhrianda, and H. R. Glyde, *Phys. Rev. B* **97**, 014513 (2018).
- [12] A. Del Maestro and I. Affleck, *Phys. Rev. B* **82**, 060515(R) (2010).
- [13] F. D. M. Haldane, *Phys. Rev. Lett.* **47**, 1840 (1981).
- [14] J. K. Freericks and H. Monien, *Europhys. Lett.* **26**, 545 (1994).
- [15] N. Elstner and H. Monien, *Phys. Rev. B* **59**, 12184 (1999).
- [16] G. G. Batrouni and R. T. Scalettar, *Phys. Rev. B* **46**, 9051 (1992).
- [17] V. Kashurnikov, A. Krasavin, and B. Svistunov, *JETP Lett.* **64**, 99 (1996).
- [18] G. G. Batrouni, R. T. Scalettar, and G. T. Zimanyi, *Phys. Rev. Lett.* **65**, 1765 (1990).
- [19] R. V. Pai, R. Pandit, H. R. Krishnamurthy, and S. Ramasesha, *Phys. Rev. Lett.* **76**, 2937 (1996).
- [20] T. D. Kühner and H. Monien, *Phys. Rev. B* **58**, R14741 (1998).
- [21] T. D. Kühner, S. R. White, and H. Monien, *Phys. Rev. B* **61**, 12474 (2000).
- [22] C. Kollath, U. Schollwöck, J. von Delft, and W. Zwerger, *Phys. Rev. A* **69**, 031601(R) (2004).
- [23] L. Urba, E. Lundh, and A. Rosengren, *J. Phys. B* **39**, 5187 (2006).
- [24] S. Ejima, H. Fehske, and F. Gebhard, *Europhys. Lett.* **93**, 30002 (2011).
- [25] M. Pino, J. Prior, A. M. Somoza, D. Jaksch, and S. R. Clark, *Phys. Rev. A* **86**, 023631 (2012).
- [26] S.-D. Ouyang, J. Liu, S.-H. Xiang, and K.-H. Song, *Chin. Phys. Lett.* **30**, 086701 (2013).
- [27] M. Gerster, M. Rizzi, F. Tschirsich, P. Silvi, R. Fazio, and S. Montangero, *New J. Phys.* **18**, 015015 (2016).
- [28] W. Koller and N. Dupuis, *J. Phys.: Condens. Matter* **18**, 9525 (2006).
- [29] S. Ejima, H. Fehske, F. Gebhard, K. zu Münster, M. Knap, E. Arrigoni, and W. von der Linden, *Phys. Rev. A* **85**, 053644 (2012).
- [30] V. A. Kashurnikov and B. V. Svistunov, *Phys. Rev. B* **53**, 11776 (1996).
- [31] H. Saito, *J. Phys. Soc. Jpn.* **86**, 093001 (2017).
- [32] H. Saito and M. Kato, *J. Phys. Soc. Jpn.* **87**, 014001 (2018).
- [33] K. McBrien, G. Carleo, and E. Khatami, *J. Phys.: Conf. Ser.* **1290**, 012005 (2019).
- [34] J. M. Kosterlitz and D. J. Thouless, *J. Phys. C* **6**, 1181 (1973).
- [35] D. R. Nelson and J. M. Kosterlitz, *Phys. Rev. Lett.* **39**, 1201 (1977).
- [36] V. L. Berezinsky, *Sov. Phys. JETP* **34**, 610 (1972).
- [37] E. L. Pollock and D. M. Ceperley, *Phys. Rev. B* **36**, 8343 (1987).
- [38] B. Grémaud and G. G. Batrouni, *Phys. Rev. Lett.* **127**, 025301 (2021).
- [39] D. Contessi, D. Romito, M. Rizzi, and A. Recati, *Phys. Rev. Res.* **3**, L022017 (2021).
- [40] T. Giamarchi, *Quantum Physics in One Dimension* (Oxford University Press, Oxford, 2003).
- [41] M. P. A. Fisher, P. B. Weichman, G. Grinstein, and D. S. Fisher, *Phys. Rev. B* **40**, 546 (1989).
- [42] A. J. Leggett, *Rev. Mod. Phys.* **71**, S318 (1999).
- [43] G. B. Hess and W. M. Fairbank, *Phys. Rev. Lett.* **19**, 216 (1967).
- [44] D. J. Scalapino, S. R. White, and S. Zhang, *Phys. Rev. B* **47**, 7995 (1993).
- [45] S. Mukerjee and B. S. Shastry, *Phys. Rev. B* **77**, 245131 (2008).
- [46] M. E. Fisher, M. N. Barber, and D. Jasnow, *Phys. Rev. A* **8**, 1111 (1973).
- [47] T. Giamarchi and B. S. Shastry, *Phys. Rev. B* **51**, 10915 (1995).
- [48] N. V. Prokof'ev and B. V. Svistunov, *Phys. Rev. B* **61**, 11282 (2000).
- [49] S. Burger, F. S. Cataliotti, C. Fort, F. Minardi, M. Inguscio, M. L. Chiofalo, and M. P. Tosi, *Phys. Rev. Lett.* **86**, 4447 (2001).
- [50] F. S. Cataliotti, S. Burger, C. Fort, P. Maddaloni, F. Minardi, A. Trombettoni, A. Smerzi, and M. Inguscio, *Science* **293**, 843 (2001).
- [51] R. Toda, M. Hieda, T. Matsushita, N. Wada, J. Taniguchi, H. Ikegami, S. Inagaki, and Y. Fukushima, *Phys. Rev. Lett.* **99**, 255301 (2007).
- [52] H. Ikegami, Y. Yamato, T. Okuno, J. Taniguchi, N. Wada, S. Inagaki, and Y. Fukushima, *Phys. Rev. B* **76**, 144503 (2007).
- [53] J. Taniguchi, Y. Aoki, and M. Suzuki, *Phys. Rev. B* **82**, 104509 (2010).
- [54] P.-F. Duc, M. Savard, M. Petrescu, B. Rosenow, A. Del Maestro, and G. Gervais, *Sci. Adv.* **1**, e1400222 (2015).
- [55] T. Eggel, M. A. Cazalilla, and M. Oshikawa, *Phys. Rev. Lett.* **107**, 275302 (2011).
- [56] I. Danshita and A. Polkovnikov, *Phys. Rev. A* **85**, 023638 (2012).
- [57] A. Masaki-Kato, S. Yunoki, and D. S. Hirashima, *Phys. Rev. B* **100**, 224515 (2019).
- [58] D. S. Hirashima, *Phys. Rev. B* **102**, 104506 (2020).
- [59] M. Fishman, S. R. White, and E. M. Stoudenmire, [arXiv:2007.14822](https://arxiv.org/abs/2007.14822).
- [60] B. S. Shastry and B. Sutherland, *Phys. Rev. Lett.* **65**, 243 (1990).
- [61] P. Calabrese and A. Lefevre, *Phys. Rev. A* **78**, 032329 (2008).
- [62] F. Pollmann, S. Mukerjee, A. M. Turner, and J. E. Moore, *Phys. Rev. Lett.* **102**, 255701 (2009).
- [63] M. A. Cazalilla, R. Citro, T. Giamarchi, E. Orignac, and M. Rigol, *Rev. Mod. Phys.* **83**, 1405 (2011).
- [64] D. M. Gangardt and G. V. Shlyapnikov, *Phys. Rev. Lett.* **90**, 010401 (2003).

- [65] D. M. Gangardt, *J. Phys. A: Math. Gen.* **37**, 9335 (2004).
- [66] M. Rigol and A. Muramatsu, *Phys. Rev. A* **70**, 031603(R) (2004).
- [67] K. V. Krutitsky, *Phys. Rep.* **607**, 1 (2016).
- [68] M. Girardeau, *J. Math. Phys.* **1**, 516 (1960).
- [69] P. Jordan and E. Wigner, *Z. Phys.* **47**, 631 (1928).
- [70] P. Calabrese and J. Cardy, *J. Stat. Mech.* (2004) P06002.
- [71] I. Bloch, J. Dalibard, and W. Zwerger, *Rev. Mod. Phys.* **80**, 885 (2008).
- [72] C. Chin, R. Grimm, P. Julienne, and E. Tiesinga, *Rev. Mod. Phys.* **82**, 1225 (2010).
- [73] M. Łański, H. Pichler, A. Sterdyniak, A. Lyras, V. E. Lembessis, O. Al-Dossary, J. C. Budich, and P. Zoller, *Phys. Rev. A* **93**, 013604 (2016).
- [74] S. Stringari, *Phys. Rev. Lett.* **76**, 1405 (1996).
- [75] F. Zambelli and S. Stringari, *Phys. Rev. Lett.* **81**, 1754 (1998).
- [76] D. Guéry-Odelin and S. Stringari, *Phys. Rev. Lett.* **83**, 4452 (1999).
- [77] S. Stringari, *Europhys. Lett.* **65**, 749 (2004).
- [78] S. Giorgini, L. P. Pitaevskii, and S. Stringari, *Rev. Mod. Phys.* **80**, 1215 (2008).
- [79] Z.-B. Lu, J.-S. Chen, and J.-R. Li, *J. Stat. Mech.* (2012) P01020.
- [80] G. De Rosi and S. Stringari, *Phys. Rev. A* **94**, 063605 (2016).
- [81] C. D. Rossi, R. Dubessy, K. Merloti, M. de Goër de Herve, T. Badr, A. Perrin, L. Longchambon, and H. Perrin, *J. Phys.: Conf. Ser.* **793**, 012023 (2017).
- [82] S. Riedl, E. R. S. Guajardo, C. Kohstall, J. H. Denschlag, and R. Grimm, *New J. Phys.* **13**, 035003 (2011).
- [83] L. Tanzi, J. G. Maloberti, G. Biagioni, A. Fioretti, C. Gabbanini, and G. Modugno, *Science* **371**, 1162 (2021).
- [84] T. Ho and Q. Zhou, *Nat. Phys.* **6**, 131 (2010).
- [85] I. B. Spielman, *Phys. Rev. A* **79**, 063613 (2009).
- [86] Y.-J. Lin, R. L. Compton, A. R. Perry, W. D. Phillips, J. V. Porto, and I. B. Spielman, *Phys. Rev. Lett.* **102**, 130401 (2009).
- [87] N. R. Cooper and Z. Hadzibabic, *Phys. Rev. Lett.* **104**, 030401 (2010).
- [88] S. T. John, Z. Hadzibabic, and N. R. Cooper, *Phys. Rev. A* **83**, 023610 (2011).
- [89] P.-K. Chen, L.-R. Liu, M.-J. Tsai, N.-C. Chiu, Y. Kawaguchi, S.-K. Yip, M.-S. Chang, and Y.-J. Lin, *Phys. Rev. Lett.* **121**, 250401 (2018).
- [90] L. Sidorenkov, M. Tey, R. Grimm, Y.-H. Hou, L. Pitaevskii, and S. Stringari, *Nature (London)* **498**, 78 (2013).
- [91] P. Christodoulou, M. Gałka, N. Dogra, R. Lopes, J. Schmitt, and Z. Hadzibabic, *Nature (London)* **594**, 191 (2021).
- [92] K. A. Matveev and A. V. Andreev, *Phys. Rev. Lett.* **119**, 266801 (2017).
- [93] K. A. Matveev and A. V. Andreev, *Phys. Rev. Lett.* **121**, 026803 (2018).
- [94] K. A. Matveev and A. V. Andreev, *Phys. Rev. B* **98**, 155441 (2018).
- [95] K. A. Matveev and A. V. Andreev, *Phys. Rev. B* **100**, 035418 (2019).
- [96] Y. J. Chen, S. Zapperi, and J. P. Sethna, *Phys. Rev. E* **92**, 022146 (2015).
- [97] S. L. Frederiksen, K. W. Jacobsen, K. S. Brown, and J. P. Sethna, *Phys. Rev. Lett.* **93**, 165501 (2004).